Voltage Control of Antiferromagnetic Phases at Near-Terahertz Frequencies

Anthony Barra,[1,*] John Domann,[2] Ki Wook Kim,[3,4] and Greg Carman[1]
[1]Department of Mechanical and Aerospace Engineering, University of California, Los Angeles, California 90095, USA
[2]Department of Biomedical Engineering and Mechanics, Virginia Tech, Blacksburg, Virginia 24061, USA
[3]Department of Electrical and Computer Engineering, North Carolina State University, Raleigh, North Carolina 27695, USA
[4]Department of Physics, North Carolina State University, Raleigh, North Carolina 27695, USA

(Received 16 June 2017; revised manuscript received 22 November 2017; published 21 March 2018)

A method to control antiferromagnetism using voltage-induced strain is proposed and theoretically examined. Voltage-induced magnetoelastic anisotropy is shown to provide sufficient torque to switch an antiferromagnetic domain 90° either from out of plane to in plane or between in-plane axes. Numerical results indicate that strain-mediated antiferromagnetic switching can occur in an 80-nm nanopatterned disk at frequencies approaching 1 THz but that the switching speed heavily depends on the system's mechanical design. Furthermore, the energy cost to induce magnetic switching is only 450 aJ, indicating that magnetoelastic control of antiferromagnetism is substantially more energy efficient than other approaches.

DOI: 10.1103/PhysRevApplied.9.034017

I. INTRODUCTION

There is a need for energy-efficient control of magnetism at terahertz frequencies. Consequently, significant effort has been directed at controlling nanoscale magnetism by strain coupling the magnetic and electric order parameters of composites containing piezoelectric and magnetoelastic materials. Such systems are highly energy efficient, with a predicted energy cost per state switch of approximately 10 aJ [1,2], but their frequency response is limited by the magnetoelastic film's ferromagnetic resonance (usually in the range of 1–10 GHz). Antiferromagnetic materials are attractive alternatives because they exhibit resonances 2 to 3 orders of magnitude higher (approximately 1 THz) [3,4]; however, they are difficult to manipulate with external fields because the applied field needs to overcome the exchange anisotropy and induce a spin-flop transition (which usually occurs for >1 T). This paper proposes solving the 1-T control problem by leveraging magnetoelastic coupling found in antiferromagnets like NiO [5–10] or FeMn [11]. In particular, the uniaxial nature of the strain anisotropy enables rotation of the antiferromagnet phase without overcoming the antiferromagnetic exchange, and this lowers the required switching anisotropy by a factor of 10–100 times. To further analyze the dynamics in such systems, we present a numerical framework which solves the ten coupled partial differential equations that govern spatiotemporal magnetoelastic response in antiferromagnetic-piezoelectric composites and demonstrate energy-efficient ultrafast switching. This strain-mediated voltage control of magnetism offers a pathway to drive dynamic processes on chip within the terahertz band gap between radio and optical frequencies. This advancement may enable a generation of strain-coupled antiferromagnetic sensors, spin-wave devices, and systems with tunable exchange biasing. Our findings also provide a clear direction for future research efforts to find magnetoelastic antiferromagnets with low intrinsic anisotropy.

Previous modeling efforts focused on predicting magnetoelastic dynamics in ferromagnets [12–14]. These models accounted for spatial nonuniformities in both strain and magnetization, thereby providing predictions that agreed with experimental data more closely than single-spin Stoner-Wohlfarth models or micromagnetic Landau-Lifshitz-Gilbert (LLG) models that assume uniform strain (i.e., mechanically decoupled models). Magnetoelastic models have been used to analyze voltage-controlled 180° switching in magnetic nanoelements with perpendicular magnetic anisotropy [15], in-plane magnetic switching driven by selective piezostraining using patterned electrodes [16,17], and 360° control of domain-wall rotation in nickel ring structures [18] to name a few [19]. However, dynamic magnetoelastic models of antiferromagnets have received little attention, and most antiferromagnetic models focus only on the micromagnetic behavior rather than mechanical coupling effects [20,21]. In particular, micromagnetic modeling has been used to predict the behavior of exchange-biased multilayers, specifically using finite-element calculations [22] and the Monte Carlo method [23,24]. In experimental work, only magnetoelectricity in single-phase materials [25–27] and carrier-induced spin reorientation [28,29] have previously been used for

*Corresponding author.
abarra@ucla.edu

 © 2018 American Physical Society

antiferromagnetic domain control. In this paper, continuum-level numerical modeling illustrates that magnetoelasticity can provide a high-speed low-power alternative control method for microscale antiferromagnets.

II. MODEL DEVELOPMENT

In this section, we provide the equations governing the spatiotemporal evolution of an antiferromagnetic material in response to voltage-induced strain. This formalism assumes that any antiferromagnetic phase can be deconstructed into two constituent ferromagnetic sublattices which are antiferromagnetically exchange coupled and oppositely oriented in the absence of external stimuli. Each of these sublattices is further assumed to be locally magnetically saturated throughout the entire volume. The sublattice magnetic moments are described by the vector field components $m_i^{(s)}(t)$, where $i = \{1, 2, 3\}$ indicates the direction in a Cartesian coordinate system, and $s = \{1, 2\}$ indicates the sublattice. The model also assumes magneto- and electrostatics, infinitesimal strains, and neglects thermal influences.

Under these conditions, the dynamics of each magnetic sublattice follow the LLG equation [30],

$$\frac{\partial \underline{m}^{(s)}}{\partial t} = -\gamma \underline{m}^{(s)} \times \underline{H}_{\text{eff}} - \alpha \underline{m}^{(s)} \times \frac{\partial \underline{m}^{(s)}}{dt}, \tag{1}$$

where γ is the gyromagnetic ratio, $\underline{H}_{\text{eff}}$ is the effective magnetic field, $\underline{m}^{(s)}$ is the sublattice magnetization direction, and α is the Gilbert damping parameter. $\underline{H}_{\text{eff}}$ is the driving term of the magnetic dynamics in Eq. (1). It can vary in space and time, and it is determined by taking the functional derivative of the total free-energy density E_{total},

$$\underline{H}_{\text{eff}}^{(s)} = \frac{-1}{\mu_0 M_s} \frac{\partial E_{\text{total}}}{\partial \underline{m}^{(s)}}, \tag{2}$$

where μ_0 is the vacuum permeability, and M_s is the saturation magnetization. Equation 2 indicates that $\underline{H}_{\text{eff}}$ will contain a term for each magnetic anisotropy energy that contributes to E_{total}. In antiferromagnets with negligible magnetocrystalline anisotropy, the relevant energy densities are

$$E_{\text{total}} = E_{\text{ex}}^{(1)} + E_{\text{ex}}^{(2)} + E_{\text{AFM}}^{(1-2)} + E_{\text{ME}}^{(1)} + E_{\text{ME}}^{(2)}, \tag{3}$$

where E_{ex}, E_{AFM}, and E_{ME} denote the intralattice ferromagnetic exchange, the interlattice antiferromagnetic exchange, and magnetoelastic energy densities, respectively. This formulation of the energy densities assumes that all anisotropies not specifically listed in Eq. (3) are low relative to the strain-induced anisotropy. This assumption is reasonable, as many magnetoelastic ferromagnets (Ni or FeGa), ferrimagnets $[(\text{Tb}_x, \text{Dy}_{1-x}\text{Fe}_2)]$, and antiferromagnets (FeMn, MnNi, IrMn) [31–33] have low magnetocrystalline (MCA) or shape anisotropies relative to the strength of strain coupling. Including any of these smaller additional anisotropies, like MCA or shape anisotropy, would result in the formation of preferred axes of magnetic alignment (i.e., stable states) and modify the switching dynamics by adding energy wells which the strain excitation must overcome. Since these changes may be complex, the model presented here addresses only amorphous antiferromagnets that are isotropic in plane with stable states dictated by the exchange and magnetoelastic energies in Eq. (3). The form of E_{ex} used here is common in the literature $E_{\text{ex}}^{(s)} = A\nabla^2 \underline{m}^{(s)}$ [12,32], where A is the exchange stiffness. The interlattice antiferromagnetic exchange is defined by an Ising-like term $E_{\text{AFM}}^{(1)-(2)} = -J\underline{m}^{(1)}\underline{m}^{(2)}$, where J is the antiferromagnetic exchange coupling coefficient. In most antiferromagnets, J is sufficiently large that $-\underline{m}^{(1)} \approx \underline{m}^{(2)}$ [34], which cancels the dipolar fields and leads to zero demagnetization energy. The two remaining terms $E_{\text{ME}}^{(1)}$ and $E_{\text{ME}}^{(2)}$ are functions of both strain and $\underline{m}^{(s)}$,

$$E_{\text{ME}}^{(s)} = \frac{1}{2}\left(\sum_i B_1 \varepsilon_{ii}^{\text{total}} \left(m_i^{(s)} m_i^{(s)} - \frac{1}{3}\right) + \sum_{i \neq j} B_2 \varepsilon_{ij}^{\text{total}} m_i^{(s)} m_j^{(s)}\right), \tag{4}$$

where B_1 and B_2 are the first- and second-order magnetoelastic coefficients.

Next, we present the effective fields used in the model, discuss the magnetomechanical coupling terms, and examine their connection to elastodynamic behavior. The two intralattice exchange fields are represented using the conventional ferromagnetic exchange term $H_{\text{ex}}^{(s)} = 2A(\mu_0 M_s)^{-1}\nabla^2 \underline{m}^{(s)}$ [35]. In contrast, the antiferromagnetic exchange field $H_{\text{AFM}}^{(s)}$ contains terms which allow the magnetization of one sublattice to influence the other. The ith component of these fields in each sublattice, respectively, are

$$[H_{\text{AFM}}^{(1)}]_i = -\frac{J m_i^{(2)}}{\mu_0 M_s^{(1)}} \quad \text{and} \quad [H_{\text{AFM}}^{(2)}]_i = -\frac{J m_i^{(1)}}{\mu_0 M_s^{(2)}}. \tag{5}$$

To simultaneously solve the coupled magnetoelastic dynamics, two additional coupling terms are needed. One of these terms, $H_{\text{ME}}^{(s)}$, is an effective field that changes the sublattice magnetic state based on the total strain $\underline{\varepsilon}^{\text{total}}$. The ith component of $H_{\text{ME}}^{(s)}$ is

$$[H_{\text{ME}}^{(s)}]_i = -\frac{1}{\mu_0 M_s^{(s)}}\left(B_1 \varepsilon_{ii}^{\text{total}} m_i^{(s)} + \sum_{j \neq i} B_2 \varepsilon_{ij}^{\text{total}} m_j^{(s)}\right), \tag{6}$$

where summation occurs only in the second term. This paper focuses on systems with isotropic magnetostriction, a

condition which requires $\lambda_{100} = \lambda_{111} = \lambda_{110}$ and $B_1 = B_2$. Furthermore, the magnetostrictive coupling is assumed to affect each sublattice equally. This requires (1) halving the magnitude of $[H_{\mathrm{ME}}^{(s)}]_i$ in Eq. (6) in comparison to the form for ferromagnets and (2) defining $B_1^{(1)} = B_1^{(2)}$ and $B_2^{(1)} = B_2^{(2)}$. To maintain the self-consistency of the model, this reduction by half is also included in the magnetoelastic strain coupling term $\underline{\underline{\varepsilon}}^{\mathrm{ME}}$, which defines the strain caused by magnetic reorientation

$$\varepsilon_{ij}^{\mathrm{ME}} = \frac{1}{2}\lambda_s\left(\frac{3}{2}\left[m_i^{(1)}m_j^{(1)} - \frac{1}{3}\right] + \frac{3}{2}\left[m_i^{(2)}m_j^{(2)} - \frac{1}{3}\right]\right), \quad (7)$$

where λ_s is the saturation magnetostriction. In the limiting case of Eq. (7), when an antiferromagnet is uniformly magnetized, $|m_i^{(s)}m_j^{(s)}| \to 1$ and $\underline{\underline{\varepsilon}}^{\mathrm{ME}} \to \lambda_s$ along the axis of magnetization. This implies that saturation magnetostriction occurs when the two sublattices are coaxially aligned. Analogous behavior is observed in ferromagnets in the limit of magnetic saturation [30].

Equations (6) and (7) ensure that the mechanical and magnetic dynamics are coupled and can be solved simultaneously. However, the calculation of $\underline{\underline{\varepsilon}}^{\mathrm{total}}$ in Eq. (6) requires that the system's elastodynamics be considered. The governing equation of linear elastodynamics is

$$\rho\frac{\partial^2 \underline{u}}{\partial t^2} - \nabla\cdot\underline{\underline{\sigma}} = 0, \quad (8)$$

$$\underline{\underline{\sigma}} = \underline{\underline{\underline{C}}}:\underline{\underline{\varepsilon}}^{\mathrm{mech}}, \quad (9)$$

where ρ is the material density, $\underline{u}$ is the displacement, $\underline{\underline{\sigma}}$ is the elastic stress, $\underline{\underline{\underline{C}}}$ is the stiffness, and $\underline{\underline{\varepsilon}}^{\mathrm{mech}}$ is the elastic strain. The driving term in Eq. (9) is the mechanical strain $\underline{\underline{\varepsilon}}^{\mathrm{mech}}$, which is the difference between the total strain $\underline{\underline{\varepsilon}}^{\mathrm{total}}$ and the magnetic strain $\underline{\underline{\varepsilon}}^{\mathrm{ME}}$. In this paper, we also consider cases where the antiferromagnet is externally strained by a piezoelectric material, in which case, $\underline{\underline{\varepsilon}}^{\mathrm{mech}}$ becomes

$$\underline{\underline{\varepsilon}}^{\mathrm{mech}} = \underline{\underline{\varepsilon}}^{\mathrm{total}} - \underline{\underline{\varepsilon}}^{\mathrm{piezo}} - \underline{\underline{\varepsilon}}^{\mathrm{ME}}, \quad (10)$$

where $\underline{\underline{\varepsilon}}^{\mathrm{piezo}}$ is the piezostrain. The strains in Eq. (10) are directly related to the physical displacements through $\underline{\underline{\varepsilon}}^{\mathrm{total}} = \frac{1}{2}[\nabla\underline{u} + (\nabla\underline{u})^T]$.

Equations (2)–(7), (9), and (10) are inserted into Eqs. (1) and (8), resulting in nine coupled partial differential equations that govern antiferromagnetic magnetoelastic dynamics. In the case where piezoelectricity is included, one more differential equation is added to calculate the electric field distribution inside the piezoelectric layer. The coupled partial differential equations are solved simultaneously using a weighted residuals method within a finite-element framework. The finite-element solver uses implicit time stepping ($t_{\mathrm{step}}^{(\mathrm{max})} = 0.5$ ps) and a backward differentiation formula. In the antiferromagnetic volume, a cuboidal finite-element mesh is used, with a maximum element size of $2.5 \times 2.5 \times 0.57$ nm^3. This element size is chosen to capture any magnetic nonuniformities within the antiferromagnet's constituent ferromagnetic sublattices on the order of the exchange length $L_{\mathrm{ex}} = (2A_{\mathrm{ex}})/(\mu_0 M_s^2)^{1/2} \approx 3.51$ nm, while simultaneously capturing any strain variations due to effects like shear lag.

The model that we develop above is used to study the two cases shown in Figs. 1(a) and 1(b). In the first case [Fig. 1(a)], an antiferromagnetic disk with an 80 nm radius and 4 nm thickness is modeled with traction-free boundary conditions ($\underline{t} = \underline{\underline{\sigma}}\cdot\underline{n} = 0$) imposed at every surface. First, the disk's antiferromagnetic state is initialized out of plane (along e_3) and relaxed for 50 ps. Then, at $t = 0$,

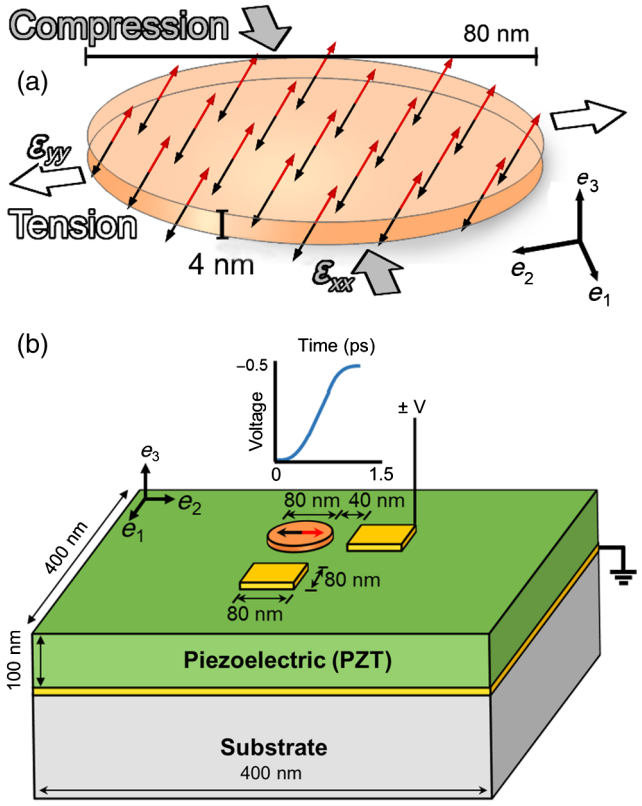

FIG. 1. The geometries used in the finite-element calculation are shown. (a) The geometry for the first model is a disk of diameter 80 nm and thickness 4 nm. The antiferromagnetic state is initially aligned out of plane, and after magnetically relaxing for 50 ps, it remains unmoved. Then, at $t = 0$, the displacement field inside the disk is precisely controlled to yield a uniform biaxial strain of 1400 $\mu\varepsilon$, with tension along e_2 and compression along e_1. (b) The geometry for the magnetomechanical model of the antiferromagnetic-piezoelectric composite is shown. In this structure, voltages can be applied at either of the two yellow electrodes (with electrical ground on the bottom planar electrode) to generate in-plane strains that can switch the antiferromagnetic state 90°. The choice of electrode dictates the eventual in-plane direction of the switched antiferromagnet.

a uniform strain field is applied everywhere in the volume, with 1000 $\mu\varepsilon$ of tension along e_2 and 400 $\mu\varepsilon$ of compression along e_1. The average sublattice magnetic response is then recorded every 0.5 ps. A Fourier analysis of the sublattice response to the broadband excitation allows for identification of the antiferromagnetic resonance frequency.

In the second model [Fig. 1(b)], an antiferromagnetic disk is attached to a thin piezoelectric film which, in turn, is attached to a thick substrate. The $400 \times 400 \times 100$ nm^3 piezoelectric film is modeled with a mechanically clamped bottom surface ($\underline{u} = 0$) and fixed in-plane boundaries ($\underline{u} \cdot n = 0$) to replicate the presence of the thick substrate and infinite extension of the film in the e_1-e_2 plane. The top surface of the composite is maintained traction-free. As in the previous model, the disk's antiferromagnetic state is first initialized out of plane and relaxed for 50 ps. After relaxation, electrical ground ($V = 0$) is applied to the piezoelectric layer's bottom surface, while a voltage excitation applied at either of the two (40×40)-nm^2 surface electrodes is ramped from 0 to -0.5 V over 1.5 ps [see Fig. 2(b) inset]. The resulting piezostrain drives magnetic precession in the disk, which is recorded every 0.5 ps. As with the previous model, these boundary conditions are chosen because they lead to high but realistic strains, like those required for switching in other magnetoelastic materials.

The material properties used for both studies are as follows (bulk values are used where the values for microscale geometries are not available, as they are known to be similar [7,36,37]). Since the material properties of magnetostrictive antiferromagnets are not well studied, the following constants are obtained from the available literature, using known constants for the ferromagnetic sublattices where relevant: $A_{ex(Fe)} \approx A_{ex(Mn)} = 2.48 \times 10^{-12}$ J/m [38], $M_{s(Fe)} \approx M_{s(Mn)} = 5.66 \times 10^5$ A/m, $\lambda_s \approx 750$ $\mu\varepsilon$ [11,39], Young's modulus $E = 77$ GPa [40], $\rho = 7700$ kg/m^3, and Poisson's ratio $\upsilon = 0.3$. A Gilbert damping parameter of $\alpha = 0.02$ is assigned to each ferromagnetic sublattice since this value is in the typical range for magnetoelastic ferromagnets [1,33,41]. With these constants, the material modeled has a likeness to $Fe_{50}Mn_{50}$, whose antiferromagnetic exchange coupling coefficient J_{AFM} is currently unmeasured. Consequently, the value of the ferromagnetic exchange coefficient of bulk single-crystal Fe $J = 3.97 \times 10^6$ J/m^3 is used. In addition, a parametric sweep of α between 0.8 and 0.02 is used to confirm that value used for the Gilbert damping parameter does not significantly influence the threshold strain required for switching for realistic values of α (<0.1). However, nonphysical high α values (>0.7) produce a strongly overdamped response that changes the antiferromagnet's mechanical impedance and reduces strain transfer across the composite interface. For this reason, low α is used. With the material parameters above, the magnetic and magnetostrictive predictions of the model cannot be quantitatively accurate for a particular material, but they are intended to represent correct trends in the material behavior and exemplify proper modeling methods. The piezoelectric layer's properties are those of transversely isotropic $Pb(Zr_xTi_{1-x})O_3$. These are $d_{13} = -6.62$ C/m^2, $d_{33} = 23.24$ C/m^2, $\rho = 7500$ kg/m^3, $E_1 = 127$ GPa, $E_2 = 82$ GPa, $G_{13} = 22.9$ GPa, $\varepsilon_{11} = \varepsilon_{22} = 3130$, and $\varepsilon_{33} = 3400$.

III. RESULTS AND DISCUSSION

Figure 2(a) shows the results for the model geometry illustrated in Fig. 1(a) after uniform strain is applied at $t = 0$ ps. The components of the Fe sublattice magnetization $m_1^{(Fe)}$ (dashed line), $m_2^{(Fe)}$ (solid line), $m_3^{(Fe)}$ (dot-dashed

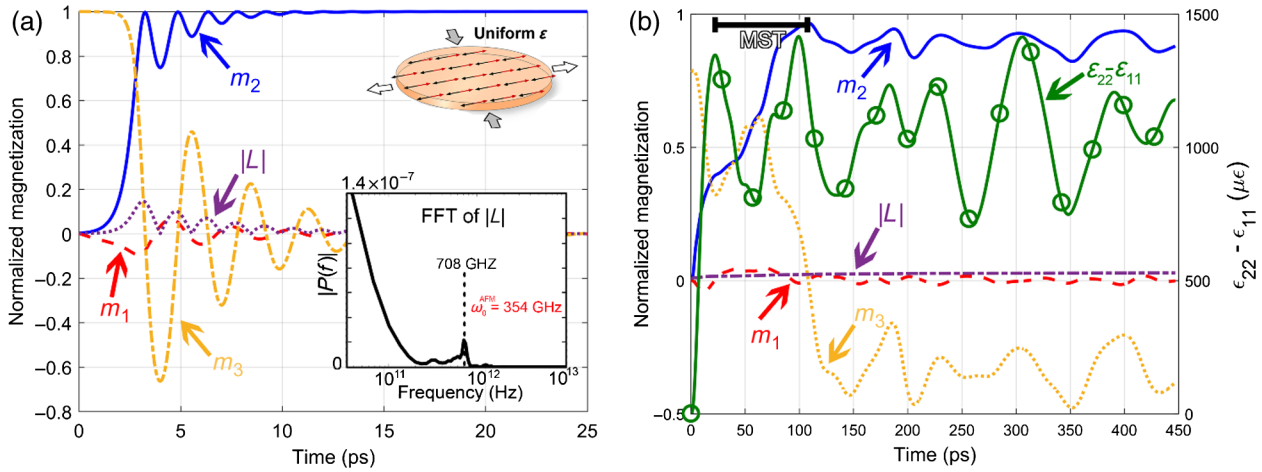

FIG. 2. The volume-averaged magnetization of the Fe sublattice is plotted in the time domain for both models. (a) When uniform biaxial strain is instantaneously applied at $t = 0$, the axis of antiferromagnetic alignment resonantly switches within 3.25 ps and settles about 12 ps later. The peak in the FFT of $|L|$ at 708 GHz corresponds with an antiferromagnetic resonance at half that value, i.e., at 354 GHz. (b) When voltage is applied at $t = 0$, antiferromagnetic switching occurs after about 100 ps. The switching process proceeds so far below resonance as to be quasistatic. The observed continuation of motion in m_2 is owed to the continuing oscillation in biaxial strain (green line), which occurs because the exciting acoustic wave internally reflects within the antiferromagnetic disk.

line), and the magnitude of the net moment $|L| = |\underline{m}^{(\mathrm{Fe})} + \underline{m}^{(Mn)}|$ (dotted line) are plotted as a function of time. The $m_2^{(\mathrm{Fe})}$ trace indicates that the sublattice realigns to the e_2 axis within 3.25 ps and then oscillates about this new orientation for approximately 10 ps before stabilizing. During the same time, $m_1^{(\mathrm{Fe})}$ and $m_3^{(\mathrm{Fe})}$ exhibit precessional decay at a lower frequency, proportional to the applied switching anisotropy. The degree of magnetic sublattice misalignment $|L|$ grows initially during the switching event in a manner proportional to $[(d\underline{m})/(dt)]$. This sublattice misalignment is caused by the uniaxial nature of the switching anisotropy, which applies oppositely pointing torques to the two sublattices. In turn, this drives the sublattices to precess to the new easy axis with opposite chirality, thereby generating a net moment that reaches a maximum of 7.3% of M_s at $t = 3.25$ ps (as $m_2^{(\mathrm{Fe})}$ saturates). In the subsequent 10 ps, L oscillates with a periodicity that matches the ringing period observed in $m_2^{(\mathrm{Fe})}$. The similarity between these periods suggests that the system relaxes through the pendulumlike motion of the two sublattices about one another at antiferromagnetic resonance. The fast Fourier transform (FFT) of $|L|$ is known to exhibit a peak at twice the antiferromagnetic resonance (AFMR). For the modeled system, this peak occurs at 0.708 THz [shown in the inset of Fig. 2(a)], which corresponds with a model-predicted AFMR of 0.354 THz. This simulated resonance is within about 28% of that predicted by theory [32]. The FFT also exhibits some high-amplitude low-frequency content, which is attributed to the amplitude decay envelope of $|L|$.

Figure 2(b) shows the results for the voltage-actuated piezoelectric and antiferromagnetic composite model [from Fig. 1(b)]. In this model, voltage is applied at $t = 0$ ps at the leftmost electrode in Fig. 1. The values of $\underline{m}^{(Fe)}$ and $|L|$ are plotted together with the volume-averaged biaxial strain state ($\varepsilon_{22} - \varepsilon_{11}$) in the antiferromagnetic disk (on the right ordinate axis). Prior to the application of voltage (i.e., during the magnetic relaxation period $t < 0$), magnetoelastic torqueing occurs due to mechanical shear lag effects at the disk edges [12], producing a nonuniform initial sublattice magnetization state with the volume-averaged components $\underline{m}^{(\mathrm{Fe})} = (0, 0, 0.78)$. Then, voltage is applied at $t = 0$, and it takes 18.5 ps for the voltage-induced strain wave to propagate from the electrode to the edge of the antiferromagnetic disk, as indicated by the first peak in the $\varepsilon_{22} - \varepsilon_{11}$ plot. It takes an additional 84 ps [labeled magnetic switching time, or MST, in Fig. 2(b)] for the strain to propagate across the disk and cause 90° rotation of $\underline{m}^{(Fe)}$. This is seen by the peak of $m_2^{(\mathrm{Fe})}$ concurring with the second peak in $\varepsilon_{22} - \varepsilon_{11}$. Throughout the MST, $m_3^{(\mathrm{Fe})}$ decays towards zero, as expected, but does not settle completely due to the system's continued strain oscillations. In contrast, $m_1^{(\mathrm{Fe})}$ remains relatively constant near zero during switching, since the switching occurs primarily in the e_2-e_3 plane. $|L|$ remains stable around <2%, and, in contrast with the uniform strain model, it does not vary with $[(d\underline{m})/(dt)]$ in the early part of the MST. These small values of $|L|$ indicate that the voltage-induced switching proceeds below the antiferromagnetic resonance (i.e., near adiabatically [42]), a phenomena also not observed in the uniformly strained model [Fig. 2(a)]. Subsequent Fourier analysis of $|L|$ indicates a broadband low-frequency response, which confirms the quasistatic nature of the switching. Further simulations show that subsequent voltage application to the other top surface electrode in Fig. 1(b) results in 90° in-plane switching from e_2 to e_1 with the same frequency response observed during out-of-plane to in-plane switching.

The comparatively slow switching speed of the antiferromagnetic-piezoelectric composite is explained by observing the spin and strain states at two different times, as shown in Fig. 3. In Figs. 3(a) and 3(b), for $t = 71.5$ ps and $t = 102.5$ ps, respectively, three-dimensional plots of strain and magnetization are provided from a perspective view (top) and a cross-sectional view (bottom). In Fig. 3(a), the strain wave during the MST, as indicated by the color gradient from red to blue (high strain is red, low strain is blue), reaches the middle of the disk. At the same time, the magnetic moments in the strained portion of the disk rotate in plane, as shown by red ($\underline{m}^{(Fe)}$) and black ($\underline{m}^{(Mn)}$) arrows, whereas the moments in the unstrained portion of the disk do not move. By the end of the MST, Fig. 3(b) shows that the strain propagates through the entire disk, and, correspondingly, the magnetization rotates uniformly in plane. Therefore, it is evident that the speed of antiferromagnetic reorientation is dictated by the speed at which strain can propagate through the disk.

While the uniform strain model suggests that near-terahertz switching in an antiferromagnet is possible, the results from the composite model indicate that for realistic strain-actuated structures, consideration must be given to the

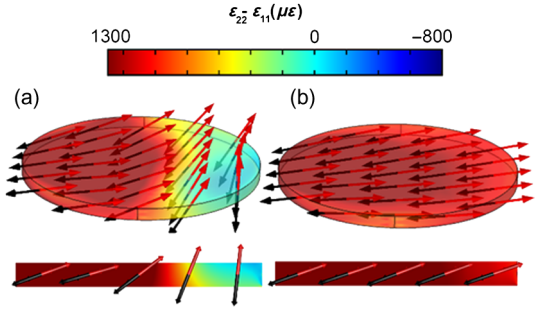

FIG. 3. The strain (3D color plot) and spin states (black and red arrows) of the antiferromagnetic disk in the composite are plotted two different times in the MST. (a) At $t = 71.5$ ps, the wave front of the acoustic excitation reaches about halfway across the disk, and the sublattice moments behind the wave front switch in plane, whereas the moments ahead of the wave front do not. (b) At $t = 102.5$ ps, the strain propagates across the disk and switches it completely.

method of mechanical actuation. In particular, the two models presented here illustrate that (1) terahertz switching is possible, (2) device design choices like the location of the actuating electrode can influence switching speed, and (3) fully coupled magnetomechanical models are necessary to predict the frequency response of strain-controlled antiferromagnets. The results presented here do not mandate that realistic devices be limited to frequencies far below antiferromagnetic resonance. For example, reducing an antiferromagnet's dimension in the direction of mechanical wave propagation should increase operational frequency. Since an antiferromagnet's thickness is commonly its shortest dimension, colocating the actuating electrode underneath it may increase switching speed up to 20 times.

Furthermore, the energy required to operate at these frequencies can be low. The energy cost per state switch is calculated from the model by numerically integrating the applied charge density over the electrode surface and then using $E_{\text{switch}} = QV/2$ to find the energy stored capacitively in the piezoelectric layer. We find that 450 aJ is sufficient to switch the axis of antiferromagnetic alignment 90°. This is 3 orders of magnitude less energy costly than alternative magnetic control methods, like spin-transfer torque, which requires 100 fJ/state switch [43].

IV. CONCLUSION

In conclusion, a fully coupled finite-element model incorporating micromagnetics, elastodynamics, and piezoelectricity is developed to predict voltage-induced magnetoelastic switching behavior in antiferromagnets. The results demonstrate that the frequency of antiferromagnetic switching can approach terahertz, but the speed is influenced by the transient of the mechanical excitation. Furthermore, the energy cost associated with controlling antiferromagnetism using strain is extremely low (100's of attojoules). This combination of high speed and low-power control may offer a development avenue for next-generation devices.

ACKNOWLEDGMENTS

This material is based upon work supported by or in part by the U.S. Army Research Laboratory and the U.S. Army Research Office under Grant No. W911NF-17-0364. This work is also supported by the NSF Nanosystems Engineering Research Center for Translational Applications of Nanoscale Multiferroic Systems under the Cooperative Agreement Grant No. EEC-1160504.

[1] Q. Wang, X. Li, C. Y. Liang, A. Barra, J. Domann, C. S. Lynch, A. Sepulveda, and G. P. Carman, Strain-mediated 180° switching in CoFeB and Terfenol-D nanodots with perpendicular magnetic anisotropy, Appl. Phys. Lett. **110**, 102903 (2017).

[2] N. D'Souza, M. Salehi Fashami, S. Bandyopadhyay, and J. Atulasimha, Experimental clocking of nanomagnets with strain for ultralow power Boolean logic, Nano Lett. **16**, 1069 (2016).

[3] Y. Mukai, H. Hirori, T. Yamamoto, H. Kageyama, and K. Tanaka, in *Proceedings of the 2015 Conference on Lasers Electro-Optics (CLEO), San Jose, CA* (IEEE, New York, 2015), p. 4.

[4] H. Kondoh, Antiferromagnetic resonance in NiO in far-infrared region, J. Phys. Soc. Jpn. **15**, 1970 (1960).

[5] L. Alberts and E. W. Lee, Magnetostriction in antiferromagnetic nickel oxide, Proc. Phys. Soc. London **78**, 728 (1961).

[6] J. P. Domann, W. Y. Sun, L. T. Schelhas, and G. P. Carman, Strain-mediated multiferroic control of spontaneous exchange bias in Ni-NiO heterostructures, J. Appl. Phys. **120**, 143904 (2016).

[7] L. Alberts and E. W. Lee, Magnetostriction in antiferromagnetic nickel oxide, Proc. Phys. Soc. London **78**, 728 (1961).

[8] P.-d.-V. du Plessis, S. J. van Tonder, and L. Alberts, Magnetostriction of a NiO single crystal. II., J. Phys. C **4**, 2565 (1971).

[9] T. Yamada, S. Saito, and Y. Shimomura, Magnetic anisotropy, magnetostriction, and magnetic domain walls in NiO. II. Experiment, J. Phys. Soc. Jpn. **21**, 672 (1966).

[10] T. R. McGuire and W. A. Crapo, Magnetic susceptibility and magnetostriction of CoO, MnO, and NiO, J. Appl. Phys. **33**, 1291 (1962).

[11] A. He, T. Ma, J. Zhang, W. Luo, and M. Yan, Antiferromagnetic $Mn_{50}Fe_{50}$ wire with large magnetostriction, J. Magn. Magn. Mater. **321**, 3778 (2009).

[12] C. Y. Liang, S. M. Keller, A. E. Sepulveda, A. Bur, W. Y. Sun, K. Wetzlar, and G. P. Carman, Modeling of magnetoelastic nanostructures with a fully coupled mechanical-micromagnetic model, Nanotechnology **25**, 435701 (2014).

[13] J. X. Zhang and L. Q. Chen, Phase-field model for ferromagnetic shape-memory alloys, Philos. Mag. Lett. **85**, 533 (2005).

[14] J. M. Hu, G. Sheng, J. X. Zhang, C. W. Nan, and L. Q. Chen, Phase-field simulation of strain-induced domain switching in magnetic thin films, Appl. Phys. Lett. **98**, 112505 (2011).

[15] X. Li, D. Carka, C. Y. Liang, A. E. Sepulveda, S. M. Keller, P. K. Amiri, G. P. Carman, and C. S. Lynch, Strain-mediated 180° perpendicular magnetization switching of a single domain multiferroic structure, J. Appl. Phys. **118**, 014101 (2015).

[16] C. Y. Liang, S. M. Keller, A. E. Sepulveda, W. Y. Sun, J. Cui, C. S. Lynch, and G. P. Carman, Electrical control of a single magnetoelastic domain structure on a clamped piezoelectric thin film–analysis, J. Appl. Phys. **116**, 123909 (2014).

[17] J. Cui, J. L. Hockel, P. K. Nordeen, D. M. Pisani, C. Y. Liang, G. P. Carman, and C. S. Lynch, A method to control magnetism in individual strain-mediated magnetoelectric islands, Appl. Phys. Lett. **103**, 232905 (2013).

[18] H. Sohn, M. E. Nowakowski, C. Y. Liang, J. L. Hockel, K. Wetzlar, S. Keller, B. M. McLellan, M. A. Marcus, A. Doran, A. Young, and M. Kläui, Electrically driven magnetic domain wall rotation in multiferroic heterostruc-

tures to manipulate suspended on-chip magnetic particles, ACS Nano **9**, 4814 (2015).
[19] C. Chen, A. Barra, A. Mal, G. Carman, and A. Sepulveda, Voltage induced mechanical/spin wave propagation over long distances, Appl. Phys. Lett. **110**, 072401 (2017).
[20] Y. G. Semenov, X. L. Li, and K. W. Kim, Currentless reversal of Néel vector in antiferromagnets, Phys. Rev. B **95**, 014434 (2017).
[21] D. Suess, T. Schrefl, W. Scholz, J. V. Kim, R. L. Stamps, and J. Fidler, Micromagnetic simulation of antiferromagnetic/ferromagnetic structures, IEEE Trans. Magn. **38**, 2397 (2002).
[22] D. Suess, M. Kirschner, T. Schrefl, J. Fidler, R. L. Stamps, and J.-V. Kim, Exchange bias of polycrystalline antiferromagnets with perfectly compensated interfaces, Phys. Rev. B **67**, 054419 (2003).
[23] P. Miltényi, M. Gierlings, J. Keller, B. Beschoten, G. Güntherodt, U. Nowak, and K. D. Usadel, Diluted Antiferromagnets in Exchange Bias: Proof of the Domain State Model, Phys. Rev. Lett. **84**, 4224 (2000).
[24] U. Nowak, A. Misra, and K. D. Usadel, Domain state model for exchange bias, J. Appl. Phys. **89**, 7269 (2001).
[25] G. T. Rado, Mechanism of the Magnetoelectric Effect in an Antiferromagnet, Phys. Rev. Lett. **6**, 609 (1961).
[26] G. T. Rado and V. J. Folen, Observation of the Magnetically Induced Magnetoelectric Effect and Evidence for Antiferromagnetic Domains, Phys. Rev. Lett. **7**, 310 (1961).
[27] N. Wu, X. He, A. L. Wysocki, U. Lanke, T. Komesu, K. D. Belashchenko, C. Binek, and P. A. Dowben, Imaging and Control of Surface Magnetization Domains in a Magnetoelectric Antiferromagnet, Phys. Rev. Lett. **106**, 087202 (2011).
[28] F. Máca, J. Mašek, O. Stelmakhovych, X. Martí, H. Reichlová, K. Uhlířová, P. Beran, P. Wadley, V. Novák, and T. Jungwirth, Room-temperature antiferromagnetism in CuMnAs, J. Magn. Magn. Mater. **324**, 1606 (2012).
[29] M. J. Grzybowski, P. Wadley, K. W. Edmonds, R. Beardsley, V. Hills, R. P. Campion, B. L. Gallagher, J. S. Chauhan, V. Novak, T. Jungwirth, and F. Maccherozzi, Imaging Current-Induced Switching of Antiferromagnetic Domains in CuMnAs, Phys. Rev. Lett. **118**, 057701 (2017).
[30] R. C. O'Handley, *Modern Magnetic Materials: Principles and Applications* (Wiley Interscience, New York, NY, USA, 2000).
[31] T. L. Gilbert, A phenomenological theory of damping in ferromagnetic materials, IEEE Trans. Magn. **40**, 3443 (2004).
[32] J. M. D. Coey, *Magnetism and Magnetic Materials* (Cambridge University Press, Cambridge, UK, 2010).
[33] D. B. Gopman, J. W. Lau, K. P. Mohanchandra, K. Wetzlar, and G. P. Carman, Determination of the exchange constant of $Tb_{0.3}Dy_{0.7}Fe_2$ by broadband ferromagnetic resonance spectroscopy, Phys. Rev. B **93**, 064425 (2016).
[34] C. Kittel, Theory of antiferromagnetic resonance, Phys. Rev. **82**, 565 (1951).
[35] A. Vansteenkiste and B. Van De Wiele, MuMax: A new high-performance micromagnetic simulation tool, J. Magn. Magn. Mater. **323**, 2585 (2011).
[36] A. Navabi, C. Chen, A. Barra, M. Yazdani, G. Yu, M. Montazeri, M. Aldosary, J. Li, K. Wong, Q. Hu, and J. Shi, Efficient Excitation of High-Frequency Exchange-Dominated Spin Waves in Periodic Ferromagnetic Structures, Phys. Rev. Applied **7**, 034027 (2017).
[37] I. Gilbert, A. C. Chavez, D. T. Pierce, J. Unguris, W. Y. Sun, C. Y. Liang, and G. P. Carman, Magnetic microscopy and simulation of strain-mediated control of magnetization in PMN-PT/Ni nanostructures, Appl. Phys. Lett. **109**, 162404 (2016).
[38] J. Du Shiming Zhou and L. Sun, *Handbook of Spintronics* (Springer Science, Dordrecht, Netherlands, 2016), p. 253.
[39] T. Ma, J. Zhang, A. He, and M. Yan, Improved magnetostriction in cold-rolled and annealed $Mn_{50}Fe_{50}$ alloy, Scr. Metall. Mater. **61**, 427 (2009).
[40] J. T. Lenkkeri, Measurements of elastic moduli of face-centred cubic alloys of transition metals, J. Phys. F **11**, 1991 (1981).
[41] M. Barangi and P. Mazumder, Straintronics-based magnetic tunneling junction: Dynamic and static behavior analysis and material investigation, Appl. Phys. Lett. **104**, 162403 (2014).
[42] J. Hong, B. Lambson, S. Dhuey, and J. Bokor, Experimental test of Landauers principle in single-bit operations on nanomagnetic memory bits, Sci. Adv. **2**, e1501492 (2016).
[43] K. L. Wang, J. G. Alzate, and P. Khalili Amiri, Low-power non-volatile spintronic memory: STT-RAM and beyond, J. Phys. D **46**, 074003 (2013).